DOI: 10.24352/UB.OVGU-2019-014 TECHNISCHE MECHANIK, 39, 1, (2019), 149 – 161
submitted: July 6, 2018

Modelling of Spark Ignition in Turbulent Reacting Droplet-laden Temporally Evolving Jet using LES

J. Stempka, L. Kuban, A. Tyliszczak

The turbulent jet flames in fuel sprays are of a great importance and are used in many practical applications, e.g., aircraft and automotive direct fuel injection systems. In this work we analyse the process of spark ignition in two-phase temporally evolving jet which carries the fuel spray. We focus on a dependence of the ignition on local flow structures, spark parameters and fuel droplets size. The fuel (n-Heptane) spray evaporates and mixes with the co-flowing oxidizer (air) creating a flammable mixture. The spark is modelled as a source term added to the energy equation. The goal of the research is to investigate the forced ignition and subsequent flame propagation/extinction in the low Mach number turbulent flow. The computations are carried out using Implicit Large Eddy Simulation (ILES) method by the high-order in-house LES solver. Liquid droplets are modelled in Lagrangian reference frame as point sources of mass, momentum and energy. The results show that combined effect of local fuel concentration, strain rate and scalar dissipation rate plays a main role in ignition. On the other hand, high rates of strain at the spark position cause substantial flame stretching leading to its extinction.

1 Introduction

Recent experimental and numerical research of reacting two-phase flows that comprise dispersed fuel spray and gaseous carrier medium have led to the new developments in combustion science. Advances help to improve overall efficiency of practical devices (e.g., gas turbines, jet engines and automotive internal combustion engines) and promote reduction of pollutant combustion products (fuel-lean operation, reheat systems). With the advent of expansion of the computational resources more advanced and realistic numerical simulations are now reachable. From that reason the numerical results of spray combustion appear more frequently in last years. Such analyses are desirable since such processes are highly complicated and not yet fully understood. Because of a large complexity of turbulent spray combustion, experimental research in this field is mostly limited to the fundamental studies. Some new and more detailed analyses has appeared recently (Mastorakos (2016); O'Loughlin and Masri (2011)). Such experiments often require very sophisticated measuring apparatus and therefore, the numerical simulations facilitate further research. Predominantly two numerical approaches are used to study such phenomena, i.e, direct numerical simulations (DNS) (Neophytou et al. (2010)) and large eddy simulations (LES) (Jones and Prasad (2010); Kuban et al. (2017); Stempka (2018)). The DNS provides detailed insight into the turbulent, reacting two-phase flows but, due to high computational cost, it is limited mainly to low Reynolds number flows and simplified domains. Thus, the LES boosts further advancements in spray combustion research since the computing demands are much lower which allows broadening the range of modelled physical phenomena. In the current work the numerical study of the forced ignition in the temporally evolving jet carrying fuel spray is undertaken. A relative motion, between the jet carrying fuel spray and external air co-flow, is imposed by a hyperbolic tangent velocity profile. The simplified configuration reduces the computational effort and allows to investigate the flow-flame interactions typical for real cases. The goal of the current work is threefold, for different initial flow fields: (i) to asses an effect of droplets spray on the flow and flame structure, (ii) to explore the relevance of spark position on ignition and (iii) to recognize causes of the flame extinction. An in-house numerical LES solver (Tyliszczak (2016)) is used to carry out the computations. It is based on high-order compact differences spatial discretisation and predictor-corrector time integration schemes. The continuous flow field is defined in Eulerian manner while the discrete phase is tracked in the Lagrangian framework. In spite of the fact that various strategies for capturing sub-grid turbulence-combustion interactions can be employed along with the sophisticated solving techniques such as: Lagrangian Particles, transported PDFs with Monte Carlo solving method, a simpler approach, namely Implicit LES (ILES) (Duwig et al. (2011)) is used for modelling the reaction kinetics. A global one-step mechanism is applied with the reaction rates calculated based on filtered values. The ILES was proven (Duwig et al. (2011)) to provide reliable solutions as far as adequate spatial resolution is achieved. The chemical reaction is initiated by

additional source term in the enthalpy equation, imitating the electrical spark (energy deposition model of Lacaze et al. (2009)).

2 Mathematical Model

The Favre-filtered continuity and Navier-Stokes equations in the framework of LES for two-phase low Mach number flows are given as:

$$\frac{\partial \bar{\rho}}{\partial t} + \frac{\partial \bar{\rho}\tilde{u}_j}{\partial x_j} = \bar{\dot{S}}_{\text{mass}}\,, \tag{1}$$

$$\frac{\partial \bar{\rho}\tilde{u}_i}{\partial t} + \frac{\partial \bar{\rho}\tilde{u}_i\tilde{u}_j}{\partial x_j} = -\frac{\partial \bar{p}}{\partial x_i} + \frac{\partial \bar{\sigma}_{ij}}{\partial x_j} + \frac{\partial \tau_{ij}^{\text{sgs}}}{\partial x_j} + \bar{\dot{S}}_{m,i}\,. \tag{2}$$

The terms appearing in Eq. (2) represent the viscous stress tensor σ_{ij} and the sub-grid stress tensor τ_{ij}^{sgs}. The latter is related to the strain rate tensor $\tilde{S}_{ij}$ by $\tau_{ij}^{\text{sgs}} = \mu_{\text{sgs}}\tilde{S}_{ij}$, where the sub-grid viscosity μ_{sgs} is calculated using the Vreman model (Vreman (2004)). The species mass fractions ($\tilde{\phi}_\alpha$) and the enthalpy (h) transport equations are given by:

$$\frac{\partial \bar{\rho}\tilde{\phi}_\alpha}{\partial t} + \frac{\partial \bar{\rho}\tilde{\phi}_\alpha\tilde{u}_j}{\partial x_j} = \frac{\partial}{\partial x_j}\left[\left(\frac{\mu}{\sigma} + \frac{\mu_{\text{sgs}}}{\sigma_{\text{sgs}}}\right)\frac{\partial \tilde{\phi}_\alpha}{\partial x_j}\right] + \bar{\dot{S}}_\alpha + \overline{\rho\dot{\omega}\left(\phi_\alpha\right)}\,, \tag{3}$$

$$\frac{\partial \bar{\rho}\tilde{h}}{\partial t} + \frac{\partial \bar{\rho}\tilde{h}\tilde{u}_j}{\partial x_j} = \frac{\partial}{\partial x_j}\left[\left(\frac{\mu}{\sigma} + \frac{\mu_{\text{sgs}}}{\sigma_{\text{sgs}}}\right)\frac{\partial \tilde{h}}{\partial x_j}\right] + \bar{\dot{S}}_h + \dot{Q}\,. \tag{4}$$

The ILES (Duwig et al. (2011)) technique is used for computing the reaction rates $\overline{\dot{\omega}\left(\phi_\alpha\right)}$, the energy deposition model (Lacaze et al. (2009)) is applied for modelling the spark source term $\dot{Q}$ and sub-grid scalar fluxes are calculated with the use of Schmidt and Schumann (1989) model. The symbol σ_{sgs} refers to the turbulent Schmidt number. Species are calculated assuming Lewis number equal to unity.

2.1 Source Terms

The dispersed phase is coupled with the flow field through the source terms appearing in Eqs. (1) to (4). They represent averaged sums of the contributions from all particles at each computational cell, i.e., $\bar{\dot{S}} = 1/\Delta^3 \sum_{p=1}^{N_p} \dot{S}_p$ where the Δ and p refer to the spatial filter width and p-th droplet, respectively. The expressions for the source terms are formulated as:

$$\bar{\dot{S}}_{\text{mass},p} = \bar{\dot{S}}_{\alpha,p} = -\frac{d}{dt}m_{d,p}\,, \tag{5}$$

$$\bar{\dot{S}}_{m,p} = -\frac{d}{dt}\left(m_d v_d\right)_p\,, \tag{6}$$

$$\bar{\dot{S}}_{h,p} = -\left(c_f m_d \frac{T - T_d}{\tau_d^T} + \frac{dm_d}{dt}h_f\right)_p\,, \tag{7}$$

$$\tau_d^T = \frac{\rho_f D_d^2}{6\text{Sh}}\frac{\text{PrLe}}{\mu_f}\frac{\text{B}_\text{T}}{ln(1+\text{B}_\text{M})}\frac{c_f}{c_{f,v}}\,, \tag{8}$$

where m_d, v_d and T_d are the droplet mass, velocity and temperature respectively, c_f and $c_{f,v}$ are the fuel and fuel's vapour heat capacities, τ_d^T is the relaxation time, h_f and μ_f are the fuel specific enthalpy of vaporization and fuel dynamic viscosity, Pr and Sh are Prandtl and Sherwood numbers and B_T and B_M represent Spalding heat and mass transfer numbers.

2.1.1 Dispersed Phase

Motion of the dispersed phase is described in Lagrangian reference frame as:

$$\frac{dx_d}{dt} = v_d\,, \tag{9}$$

$$\frac{dv_d}{dt} = \frac{\tilde{u} - v_d}{\tau_d^v}\,, \tag{10}$$

where $\tilde{u}$ is the gas phase velocity at the droplet's position, the particle relaxation time τ_d^v is expressed as

$$\frac{1}{\tau_d^v} = \frac{3}{8}\frac{\rho_f}{\bar{\rho}}\mathrm{C_D}\frac{|\bar{u} - v|}{r_d}\,, \tag{11}$$

in which the symbol $\mathrm{C_D}$ denotes the drag coefficient and r_d is the droplet radius.

2.1.2 Evaporation Model

The droplets act as point-sources of evaporating species. Following the formulation of infinite conductivity evaporation model proposed by Miller et al. (1998) the droplet temperature and mass rates of change during evaporation are computed from:

$$\frac{dT_d}{dt} = \frac{1}{3}\frac{\mathrm{Nu}}{\mathrm{Pr}}\left(\frac{c_{p,g}}{c_f}\right)\frac{T - T_d}{\tau_d^e} + \left(\frac{h_f}{c_f}\right)\frac{\dot{m}_d}{m_d}\,, \tag{12}$$

$$\frac{dm_d}{dt} = -\frac{1}{3}\frac{\mathrm{Sh}}{\mathrm{Sc}}\left(\frac{m_d}{\tau_d^e}\right)\mathrm{H_M}\,, \tag{13}$$

$$\tau_d^e = \frac{\rho_f D_d^2}{18\mu_g}\,, \tag{14}$$

where $c_{p,g}$ is the fuel vapour-gas mixture, τ_d^e is a particle relaxation time and D_d is the drop's diameter. The dimensionless numbers (Prandtl, Schmidt, Nusselt and Sherwood) are computed as $\mathrm{Pr} = \mu_g c_{p,g}/k_g$, $\mathrm{Sc} = \mu_g/\rho_g\Gamma_g$, the Nu and Sh are computed using correlations for non-stationary droplets. The $\mathrm{H_M}$ term accounts for the mass transfer potential, i.e., in the current work the "D^2 law" model (Spalding (1953)) is used and it is defined as $\mathrm{H_M} = ln\,(1 + \mathrm{B_M})$. The term $\dot{m}_d = dm_d/dt$ is the droplet mass rate of change. Physical quantities denoted by the subscript g are calculated adopting the "1/3 rule" of mixing. Such quantities are calculated at the reference temperature and mass fraction. This procedure makes them dependent on spatial and thermal variations of flow variables for the physical consistency.

2.1.3 Spark

The spark is modelled using the energy deposition (ED) model of Lacaze et al. (2009). The local amount of heat transferred into the flow during deposition is denoted as $\dot{Q}$. The contribution of the spark is accounted in the enthalpy equation as an additional source term. Energy deposition model follows the Gaussian distribution in time and space and is defined as

$$\dot{Q} = \frac{\epsilon}{4\pi^2\sigma_s^3\sigma_t}\exp^{-\frac{1}{2}\left(\frac{r}{\sigma_s}\right)^2}\exp^{-\frac{1}{2}\left(\frac{t - t_0}{\sigma_t}\right)^2}\,, \tag{15}$$

where r is the radial distance to the center of the spark, t denotes time and t_0 is the instant of time when the power density function reaches a maximum. The model is controlled by three parameters: the transmitted energy ϵ, $\sigma_s = \Delta_s/a$ and $\sigma_t = \Delta_t/a$ where Δ_s and Δ_t are characteristic size and time duration of the spark, respectively. The coefficient $a = 4\sqrt{ln\,(10)}$ is chosen so that 98% of the deposited energy finds in the domain $\Delta_s^3 \cdot \Delta_t$. The parameters describing the spark are given in Tab. 1.

Table 1: Spark parameters

Δ_s	Δ_t	t_0	ϵ	Δ_s/d_j
3 mm	0.5 ms	1.5 ms	5 mJ	0.65

The size and duration of the spark were taken based on an experimental work of Ahmed and Mastorakos (2006) devoted to analysis of an ignition probability map of methane jets. In the ED model of the spark the selected values guarantee relatively steep rise of the temperature up to the level 3500 K approximately. The time when the spark reaches the maximum intensity (t_0) corresponds to the time instance after the initial transient phase when the vortical structures start to be seen (see Fig. 7) and when small droplets start to concentrate in the vortex cores.

2.1.4 Reaction Terms

The main difference between LES and Implicit LES (ILES) relies on treatment of the reaction source terms. In ILES the sub-filter scales resulting from the filtration of the convective terms are modelled by eddy viscosity model, but the chemical source terms $\overline{\dot{\omega}(\phi_\alpha)}$ are modelled assuming $\overline{\dot{\omega}(\phi_\alpha)} \approx \dot{\omega}(\tilde{\phi_\alpha})$ (Duwig et al. (2011)). In the current analysis reaction rates are obtained from the Arrhenius formula using one-step global chemistry according to the following reaction

$$C_7H_{16} + 11(O_2 + 3.76N_2) = 7CO_2 + 8H_2O + 41N_2\,, \tag{16}$$

for which the reaction rate is tuned to give a reasonable prediction of the strain rate extinction (Fernandez-Tarrazo et al. (2006)). It was chosen to reasonably minimize the computational expense. However, this approach is known from over-predicting the flame speed for rich mixtures, yet it still can reproduce correct trends in the analysis of turbulence impact on the ignition and flame propagation without resolving the flame speed at all equivalence ratio range in details (Chakraborty and Mastorakos (2007)). The ILES assumptions would certainly fail in the Reynolds Averaged Navier-Stokes (RANS) framework as the fluctuations in RANS models are large. On the other hand, the ILES is valid for laminar flow simulation and in DNS where all turbulent flow scales are resolved. Hence, one may assume that for sufficiently dense computational meshes, when the grid cells are comparable with the Kolmogorov length scale, the ILES approach is appropriate. This is verified in preliminary computations.

3 Numerical Approach

Computations were carried out using an in-house academic LES solver for low-Mach numbers flows (SAILOR, Tyliszczak (2016)) which is based on high-order compact difference method combined with the projection method for pressure-velocity coupling on half-staggered meshes and 2$^{\text{nd}}$ order Total Variation Diminishing (TVD) scheme. Even though the low order TVD schemes are known from dumping the small-scales in the current work the scheme is used only for species convective terms discretisation to assure boundedness of the species fluxes and gave satisfactory results in the previous works (Wawrzak and Tyliszczak (2016)). Time integration is performed with the use of predictor-corrector approach as a combination of Adams-Bashforth and Adams-Moulton methods. For resolving the dispersed phase motion 1$^{\text{st}}$ order integration scheme is applied. The two-way velocity coupling is realized using 2$^{\text{nd}}$ order accurate method for the momentum source terms approximation and 4$^{\text{th}}$ degree Lagrangian polynomials for the interpolation of the flow field velocity at the droplets positions. The simulations were carried out with a varying time-step and Courant-Friedrichs-Lewy condition set to 0.1. The numerical code was thoroughly tested in the previous studies (Kuban et al. (2017); Wawrzak and Tyliszczak (2016)).

4 Configuration

The configuration used in the current study is schemtically showed in Fig. 1. The computational domain has following dimensions: $Lx = 0.025\ m$, $Ly = 0.04\ m$ and $Lz = 0.01\ m$. The periodic boundary conditions are applied in X and Z directions while the upper and lower walls are assumed adiabatic. Initially the flow, similarly as the droplets had temperatures equal to $300\ K$. The flow of the oxidizer and fuel spray is initiated by imposing hyperbolic tangent velocity profile similarly as in Hawkes et al. (2007). In effect the temporally evolving plane jet is constituted in the middle part of the domain. The jet velocity profile is defined as

$$u(y) = -\frac{U}{2} \cdot \tanh\left(\frac{d_j}{8\Theta}\left(\frac{2|y|}{d_j} - \frac{d_j}{2|y|}\right)\right)\,, \tag{17}$$

where symbol U denotes the free stream velocity of the co-flow outside the jet, $d_j = 4.6\ mm$ is the initial width of the jet and Θ denotes the momentum thickness. The Θ defines the gradient of the velocity profile at the jet edge what is shown schematically in Fig. 1. Currently the effect of two different values of Θ resulting in the ratios $d_j/\Theta = 20$ and 50 is studied among other parameters.

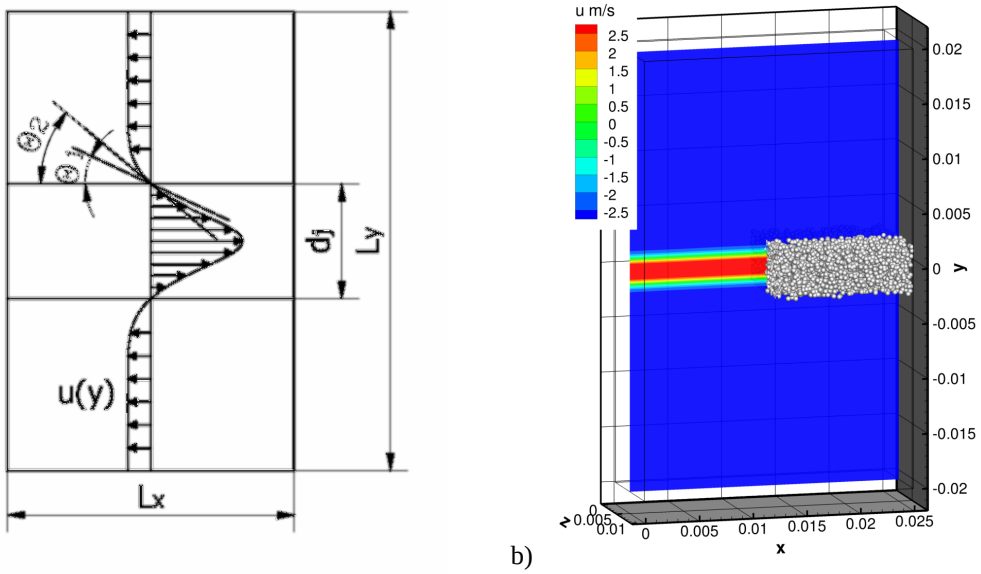

a) b)

Figure 1: (a) Scheme showing the effect on the velocity profile resulting from using two different values of Θ. (b) Computational domain at the initial state, showed are: contours of streamwise velocity and white dots indicating droplets positions (only right half).

Initially, a homogeneous isotropic turbulence field (HIT) was imposed on the flow field. The HIT is characterized by the Passot and Pouquet (1987) energy spectrum

$$E(k) = 16\sqrt{2/\pi}\frac{u'^2}{k_0}\left(\frac{k}{k_0}\right)^4 \exp^{-2\left(\frac{k}{k_0}\right)^2}, \tag{18}$$

where $u' = \left\langle\sqrt{u'u'}\right\rangle$ is the RMS of initial velocity fluctuations and k_0 is an adjustable wave number used to generate turbulent field with a required Taylor microscale $\lambda =< u'u' > / < \partial(u'u')/\partial x >$. The HIT provides temporal evolution of the jet and the velocity fluctuations are wiped out anywhere outside the jet region. The initial fluctuations for both jet Reynolds numbers Re_{d_j} studied (where $\mathrm{Re}_{d_j} = Ud_j/\nu$) were adjusted such that $\mathrm{Re}_\lambda = \lambda u'/\nu \approx 7$ while the Taylor microscales are $\lambda \approx 4e-4$ and $7e-4$ for the flows characterized by $\mathrm{Re}_{d_j} = 1000$ and 5000, respectively. In both cases the turbulence intensities are equal to $\mathrm{Ti} = 1\%$. The computational mesh consists of $120 \times 192 \times 48$ nodes distributed uniformly in each direction. The resulting grid spacings are close to $200\ \mu m$ which is comparable with the Kolmogorov length scales, i.e., $\eta_K = 125\ \mu m$ and $469\ \mu m$ for $\mathrm{Re}_{d_j} = 5000$ and 1000. Hence, it can be assumed that applied mesh of such can fulfil the ILES requirement of well stirred reactor.

The fuel (n-Heptane) spray with droplet sizes following the modified Rosin-Rammler size distribution is imposed into the middle part of the domain. Initially, the spray is distributed as a rectangular slab placed within the planar jet region and during the time it spreads due to the momentum coupling. The two distinct distributions of the droplets characterised by different Sauter mean diameters are taken into account. These are equal to (i) $d_{32} = 20\ \mu m$ with diameters within 10-30 μm range and (ii) $d_{32} = 50\ \mu m$ with diameters spreading from 20-80 μm. The initial mass loading is chosen in order to obtain a global equivalence ratio equal to $\phi = 1.5$ in each case. These resulted in liquid fuel mass loading equal to $m_f = 5.47\ g$ with two different initial number of droplets, i.e., $\mathrm{N_d} = 993372$ and 132919. Additional small portion of gaseous fuel of mass fraction equal to $\phi_f = 0.01$ is present within the jet region. The inter-droplet forces due to collisions are not taken into account because for the current study the ratio of the liquid fuel volume to that of the gaseous medium is of order 10^{-3}, which is close to the threshold value below which the droplets collisions do not strongly affect the flow (Elghobashi (1994)).

5 Results

Table 2 summarizes all investigated parameters. Each setup differs by at lest one parameter, e.g. jet Reynolds number Re_{d_j}, Sauter mean diameter d_{32} (μm) or momentum thickness Θ. Figure 2 highlights the locations of sparks events. These are labelled as (e.g. S1, S2, ..., S6) used thereafter to denote different cases. For example symbol CS4 denotes initial flow field characterised by $\mathrm{Re}_{d_j} = 5000$ with the spray for which $d_{32} = 50\ \mu m$,

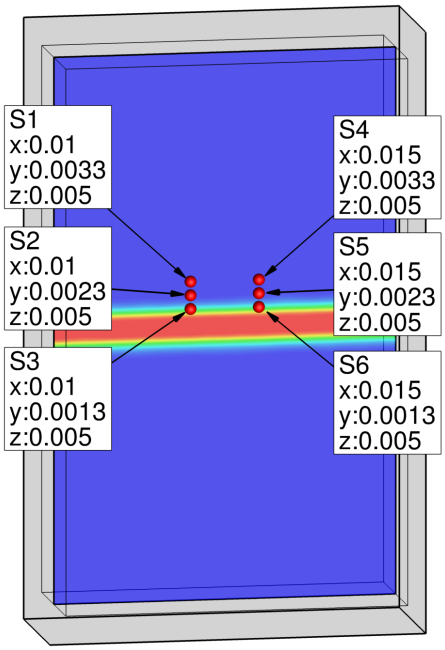

Figure 2: Picture showing spark positions with its numbering.

parameter $d_j/\Theta = 20$ and spark located at point S4 (see Fig. 2) with coordinates equal to: $x = 0.015\ m$, $y = 0.0033\ m$ and $z = 0.005\ m$. Occurrence of the ignition events for most relevant cases described in the following section are summarised in Table 3.

It can be observed that two global parameters are crucial for the successful ignition, i.e. transversal spark location and the jet Reynolds number. Comparison of the results obtained for setups A and B is shown in Figure 3 and for setups C and G in Figure 4. The plots present instantaneous local maximum temperature, fuel mass fraction and the flame volume which is defined as the volume occupied by the gas which temperature is higher than $1200\ K$. The computations of setups C to D and G to H led to analogical observations.

Apparently, the shear layer thickness d_j/Θ has marginal effect on ignition while slight change in spark location relative to the jet region along with the change of Re_{d_j} are the most influential parameters. In both cases (A and B setups) independently on the momentum thickness, sparking at the locations S3 and S6 lead to unsuccessful ignition. In opposition to locations S3 and S6 spark events in other locations result in successful ignition, (again) independently of d_j/Θ. From above results, it is seen that shifting spark location along the shear layer (x-direction) has marginal impact on likelihood of the ignition. This can be attributed to the use of temporally evolving jet rather than spatially evolving one. The turbulence intensity of HIT seems to be too weak to have a substantial impact on the flow field in different axial sparks locations. On the contrary, moving the spark transversely (y-direction) results in different ignition scenario. Changing the spark location may result either in ignition or its lack depending on the mixture composition and velocity gradient along transversal direction.

Table 2: Simulation setups

Case	Re_{d_j}	d_{32}	d_j/Θ
A	5000	20	20
B	5000	20	50
C	5000	50	20
D	5000	50	50
E	1000	20	20
F	1000	20	50
G	1000	50	20
H	1000	50	50

Table 3: Results summary

Case	S1	S2	S3
A	ignition	ignition	no ignition
B	ignition	ignition	no ignition
C	no ignition	no ignition	no ignition
D	no ignition	no ignition	no ignition
E	ignition	ignition	no ignition
F	ignition	ignition	no ignition
G	ignition	ignition	no ignition
H	ignition	ignition	no ignition

(a) Cases: AS1/AS4, AS2/AS5, AS3/AS6

(b) Cases: BS1/BS4, BS2/BS5, BS3/BS6

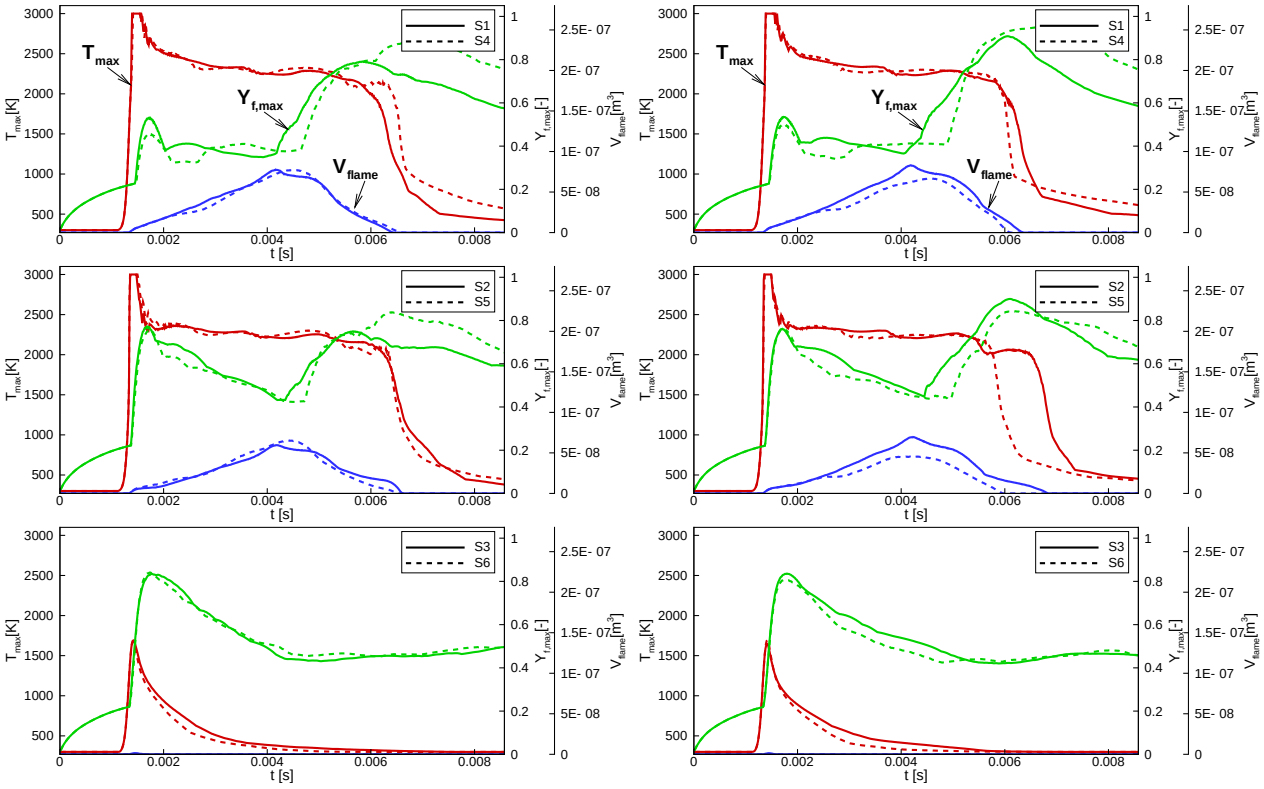

Figure 3: Plots showing instantaneous maximal temperature, fuel mass fraction and flame volume.

(a) Cases: CS1, CS2, CS3

(b) Cases: GS1, GS2, GS3

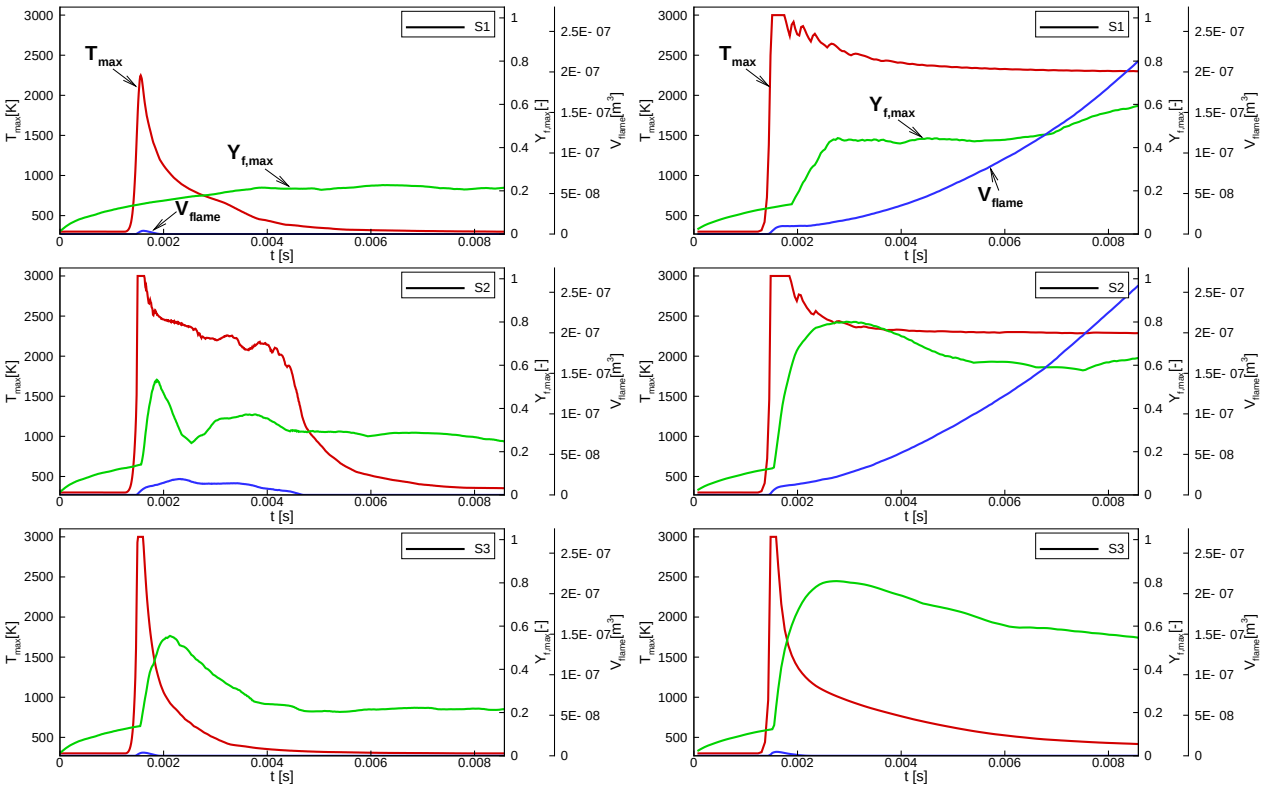

Figure 4: Plots showing instantaneous maximal temperature, fuel mass fraction and flame volume.

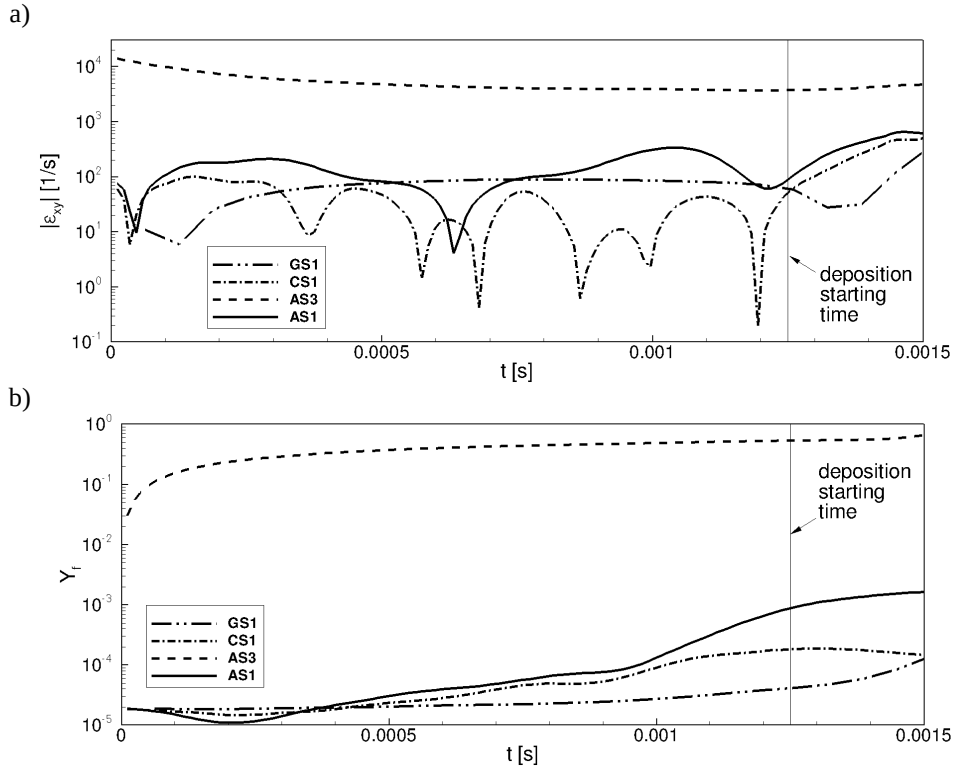

Figure 5: (a) Plot showing the instantaneous absolute values of the xy component of strain rate tensor. (b) Plot showing the instantaneous values of the local fuel mass fraction.

Figures 3a) and b) show that hot kernel survives only few Δ_t for setups A and B, excluding the S3 and S6 locations for which the flame kernel development is unsuccessful. An indication for that fact can be found in flame volume plot which shows slight growth during time period from 1.5 ms to 4 ms for which the temperature values reach maximum and then starts to fall. One can also notice that spark events in positions S3 and S6 led to only slight rise of maximal temperature comparing to positions S1, S2, S4 and S5. That could be due to the intense cooling effect of cold gas flowing in the vicinity of the spark. The heat from hot gaseous kernel is convected to the jet stream so the thermal energy deposited locally is lower than the activation energy preventing the initiation of chemical reactions. Figure 4 presents comparison of the results obtained for setups with Reynolds numbers $\mathrm{Re}_{d_j} = 5000$ (Fig. 4a) and Re_{d_j}=1000 (Fig. 4b) characterized by the same Sauter mean diameter of fuel droplets ($d_{32} = 50\ \mu m$). Evidently cases CS1, CS2, CS3 (Fig. 4a), did not succeed in ignition neither in the flame kernel initiation. On the

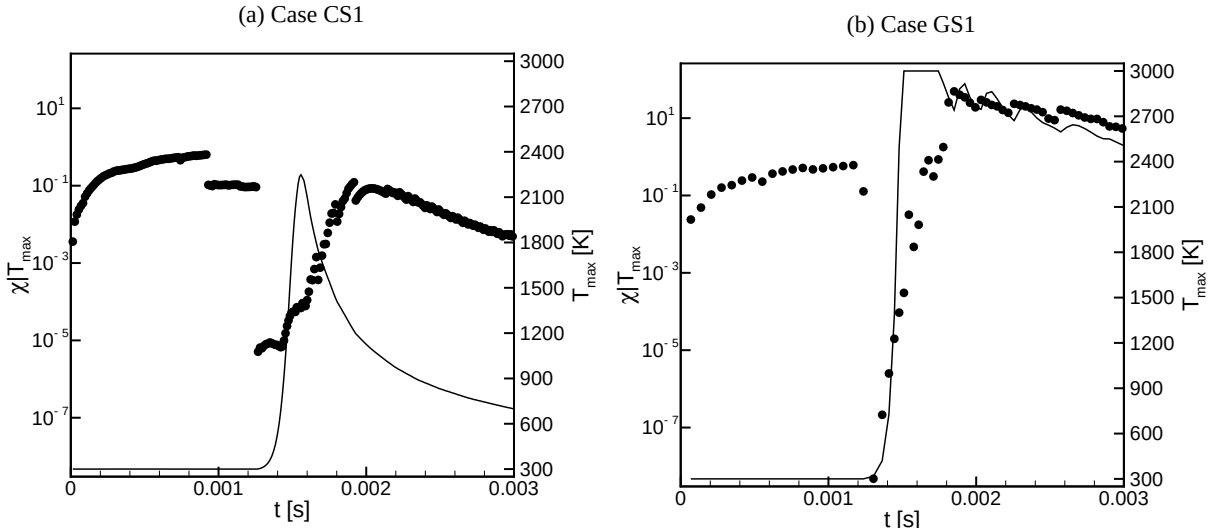

Figure 6: Plots showing time variations of scalar dissipation rate conditioned by the maximum temperature $\chi|T_{max}$ (dots) along with maximum temperature growth (lines).

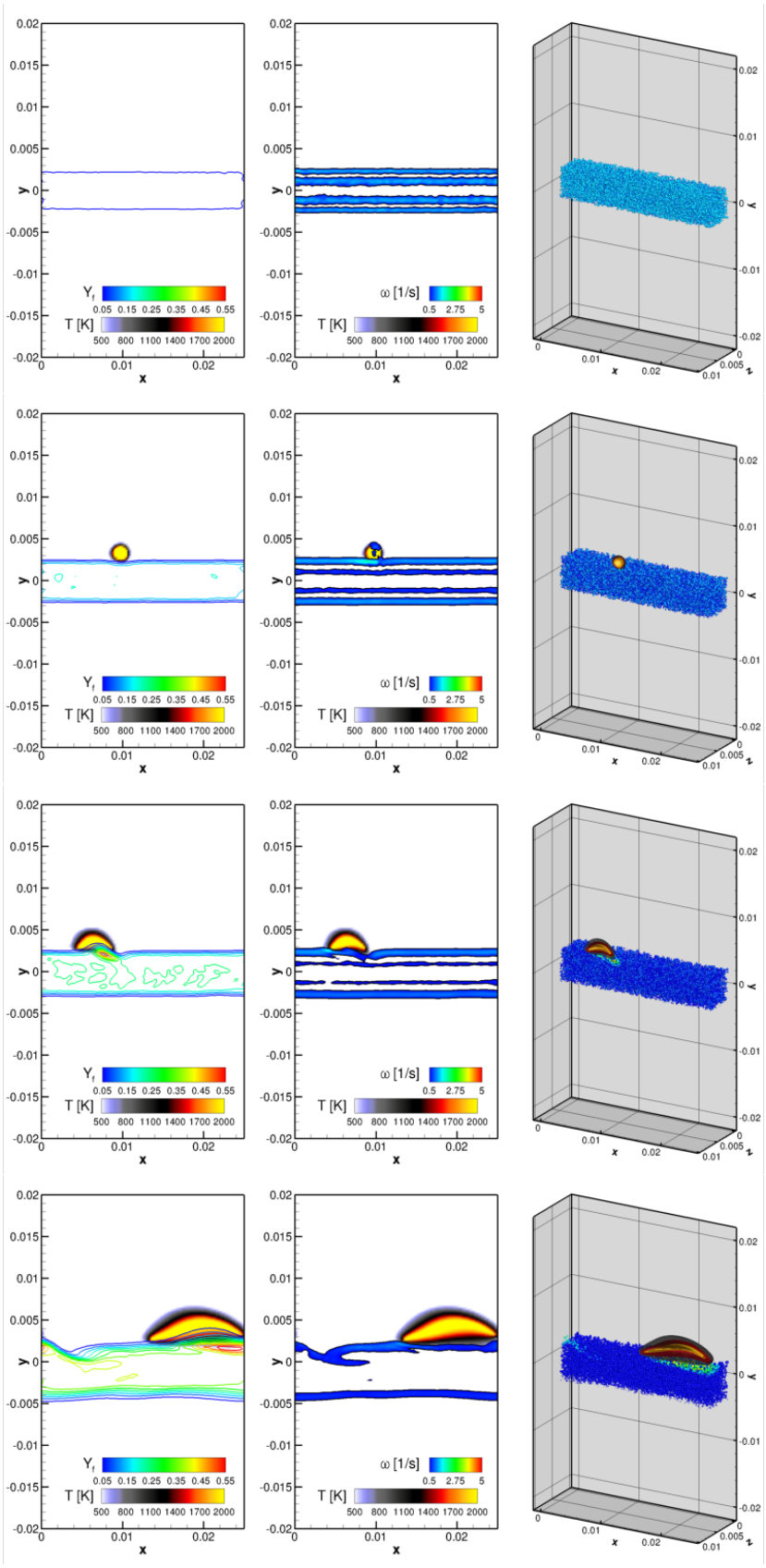

Figure 7: Contour plots of temporal evolution of temperature and vorticity magnitude with indication of spray stream depicted as spheres, showing flame initiation and propagation in setup GS1. The subfigures are given for time instances: 0.07, 0.35, 0.83 and 1.74 ms from top to the bottom one, respectively.

contrary, the cases that differ only in droplets diameter (setups AS1, AS2) have led to successful ignition. Hence, the importance of droplet diameter on ignition likelihood emerges. This agrees comparing the results of Y_f (setups A and C) for which the amount of maximum fuel content just before the energy deposition is lower when larger droplets are considered. Analysis of the isolated effect of Re_{d_j} for the same initial $d_{32} = 50\ \mu m$ (Fig. 4) leads to the observation that when larger droplets are present - ignition still may occur but only for lower Re_{d_j}. This manifests the case that the effect of evaporation rate cannot be itself viewed as the key reason for the lack of ignition. For higher Re_{d_j} three ignitions events are not successful. Steep velocity gradients cause fluid elements to strain and lead to increase in shear stresses within the shear layer between jet and co-flow thus preventing the ignition. Indeed, analysis of plots showing the instantaneous local values of strain rate tensor component ϵ_{xy} (Fig. 5a) and fuel content Y_f (Fig. 5b) before the energy deposition reveals differences in local flow conditions for cases CS1 and GS1. Monitored Y_f at the location S1 for this two setups differ only slightly, this was expected since the droplet diameters are the same while ϵ_{xy} shows completely different bahaviur for both Re_{d_j}. For higher Re_{d_j} the plot reveals highly irregular path while for lower Re_{d_j} is more smooth. Sharp oscillations of ϵ_{xy} values with amplitude of about 2 orders of magnitude preceeding the energy depostion event cause substantial straining of the hot kernel for higher Re_{d_j}. These findings are similar to the ones shown by Lacaze et al. (2009) where the effect of higher streamwise velocity on spark ignition resulted in lower ignition probability. Cases with lower Re_{d_j} (GS1, GS2) (Fig. 4b) lead to successful flame initiation and further flame propagation as can be seen from the plots of maximal temperature and flame volume. After the spark energy deposition is terminated, the maximum temperature falls slightly and reaches steady, near-adiabatic level while the flame volume continues to rise.

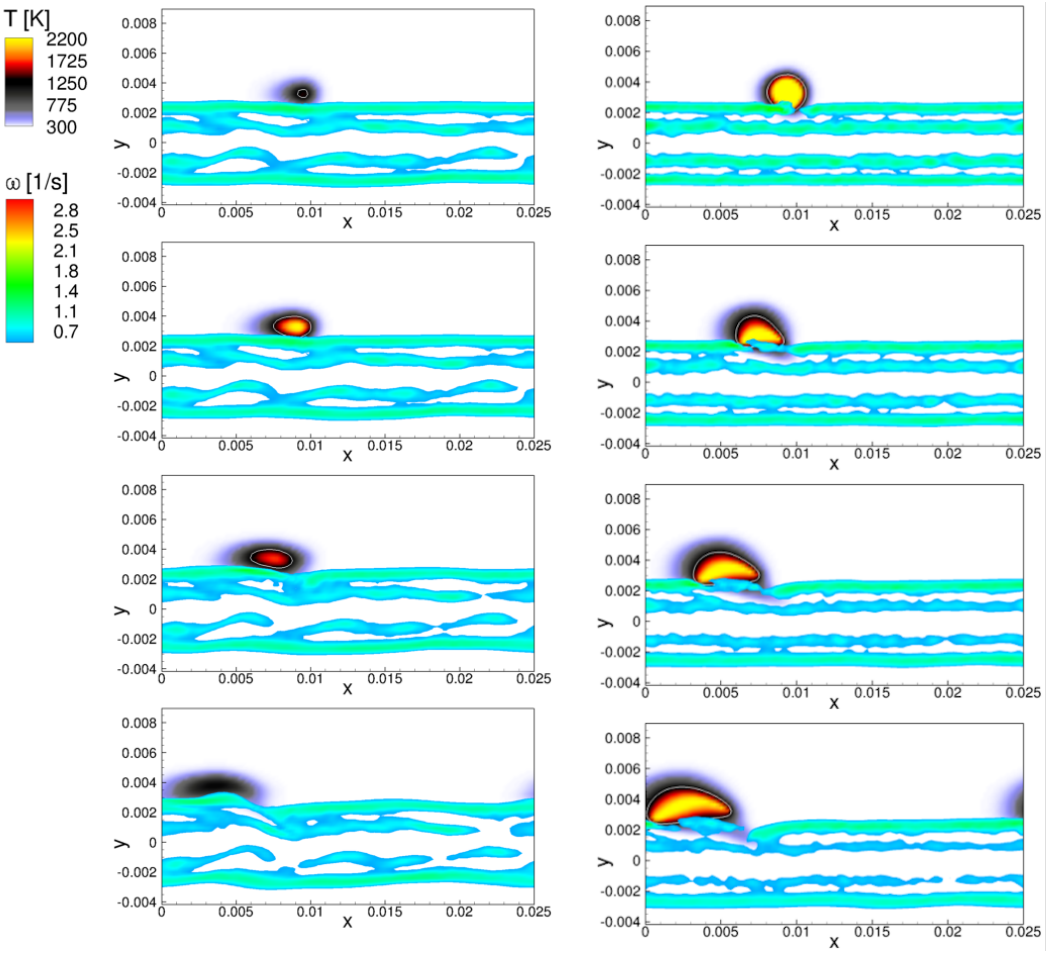

(a) (b)

Figure 8: Contours of temporal evolution of temperature and vorticity magnitude for setup: (a) CS1 and (b) GS1. The subfigures are given for time instances: 0.35, 0.48, 0.79 and 1.5 ms from top to the bottom one, respectively.

Figure 7 shows exemplary process of flame initiation and propagation in setup GS1. It is drawn along with contours of fuel mass fraction, vorticity magnitude and fuel spray indicated by the blue dots coloured by the droplets temperature. It can be seen that flame after its initiation grows in spherical manner until it starts to interact with upper edge of the slab of droplets. From that moment the thermal expansion of highly heated gas causes deviations

from spherical shape because the velocity of expanding gas is different towards the co-flow and spray. The spray also affects the flame kernel by a rapid absorption of the heat because at that side convection is intense due to higher flow rates of cold gas towards the jet axis. Flame initially can not penetrate the spray rather than that it only slides on the edge of the droplet slab being fed by weakly evaporating fuel. Flame starts to penetrate the spray after it is dispersed by large flow structures. On the other hand, the cases GS3 and CS3 result in a rapid decrease of the maximum temperature shortly after the spark event. Indicating again, that the position S3 is not suitable for igniting the mixture. This is also manifested by a very intense strain rate and high local fuel load at point S3 (see AS3 in Fig. 5). However, the major cause of a misfire in case of setup GS3 was found to be attributed to the high local fuel content when the spark is placed within droplets stream. The fuel mass fraction exceeds the upper flammability limit for n-Heptane during spark deposition. Further analysis of setups CS1 and GS1 for which the only difference was in Re_{d_j} basis on a comparison of scalar dissipation rates χ accompanying spark energy deposition. Figure 6 shows scatter plots of χ conditioned with local maximum temperature $\chi|T_{max}$. It can be seen that at the beginning of the energy deposition the $\chi|T_{max}$ are more than 2 orders of magnitude lower for GS1 than for CS1, since χ is proportional to mixture fraction gradient, it indicates that the reactants are well stirred.

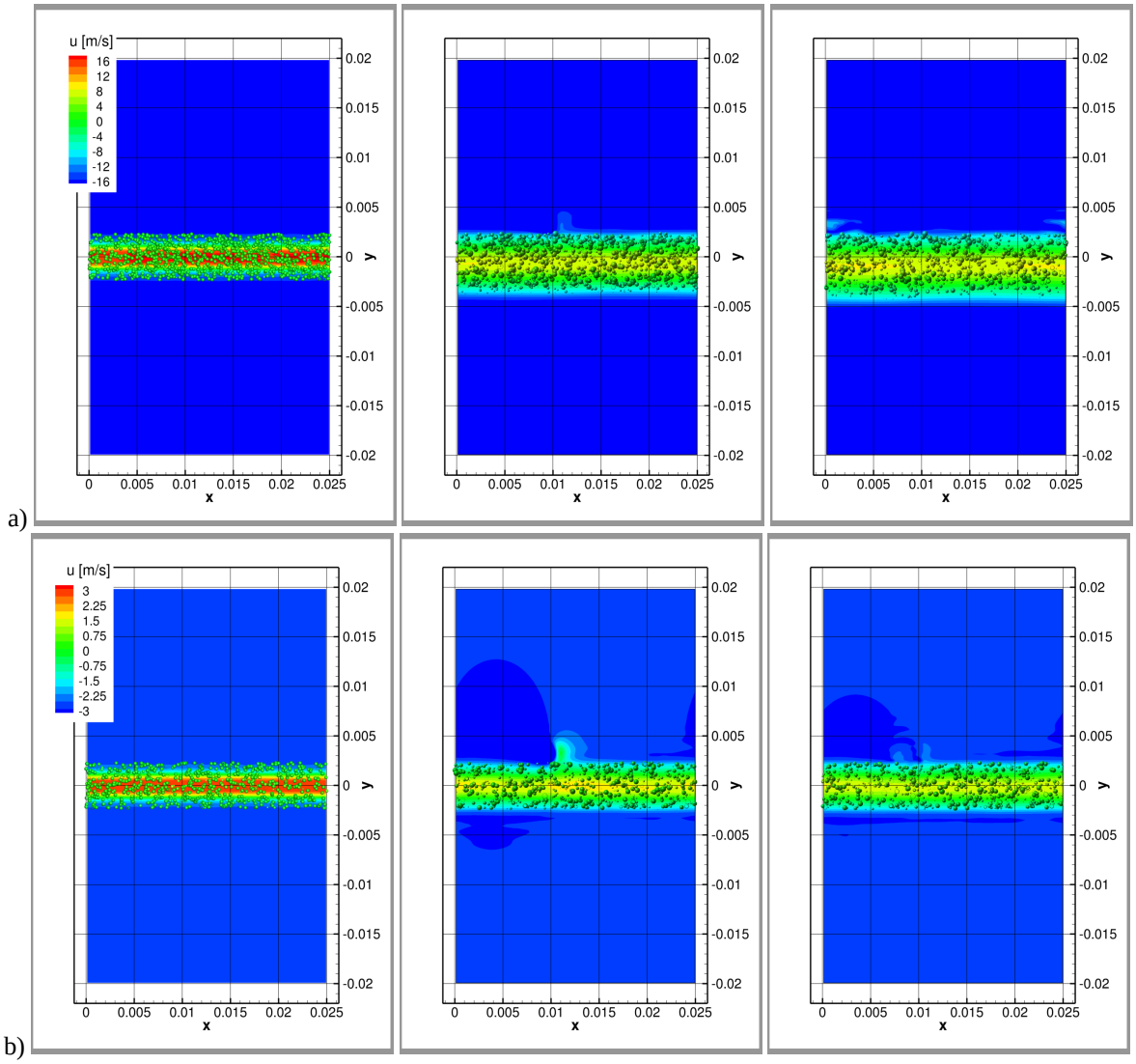

Figure 9: Contours of temporal evolution of axial velocity with imposed spray indicated by spheres of different size. Droplets are scaled with the D_d and coloured by its axial velocity component. Presented setups: (a) CS1, (b) GS1. The subfigures are given for time instances: 0.07, 1.5 and 2 ms from left to the right one, respectively.

The graphical representation of the vorticity and temperature fields presenting the flame kernel initiation (CS1) and its development (GS1) are shown in Figure 8. Initially, in both cases the flame kernel has spherical shape and is growing until reaching the jet shear layer. The kernel is further subjected to the steep velocity gradient that stretches it intensively. Being stretched by the shear forces the flame starts to propagate along the upper shear

layer. The cold jet stream of droplets as well as high velocity inside the jet cause substantial heat convection from the flame kernel so its entrance inside the fuel stream is prevented. The flame slides along the shear layer until the jet is developed and spray is more dispersed. Further, bigger flow structures start to develop within the jet. These structures along with the thermal expansion of hot gasses lead to droplet dispersion and allow the flame to penetrate the spray slab. At that point the differences between CS1 and GS1 are more pronounced. Rapid heat convection in case of setup CS1 caused by higher flow rate adjacent to the hot gas kernel causes the kernel's temperature to drop. The flame kernel of GS1 survives because the reaction is self-sustained and heat release is higher than the heat loses. This allows the flame to continue its growth primarily in the upper side of droplet slab with gradual penetration through the fuel jet.

By analysing the results from cases CS1 and GS1 shown in Figure 9 one can learn about droplet dispersion caused by the flow. Pictures of several succeeding time instances present contour plots of axial velocity with imposed spheres indicating the fuel spray which are scaled by the D_d and coloured by its axial velocity values. It can be seen that in case of higher Re_{d_j} (Fig. 9a) the inertia of the droplets is quickly overtaken by the jet stream so the spray follows the flow as it is indicated by the same colors of droplets and contours. For flow with lower Re_{d_j} (Fig. 9b) at the same time instances, the temporal development of the jet region is weaker resulting in lower spray slab width than observed for higher Re_{d_j}. It can be also noticed that at this point, the inertia of the droplets is more pronounced because even for furthest time instance the velocity differences between droplets and flow are noticeable. Both cases indicate that even at flow times two times greater than t_0 (third picture) spray is not dispersed anywhere in the domain but rather trapped by the shear layers on both sides of the jet. The initial width of the spray slab only slightly increases until later times when larger flow structures breaks the slab and throw droplets elsewhere (not shown here). This occurs faster in the case with higher Re_{d_j}. It can be also seen that smaller droplets with the smaller Stokes numbers mostly migrate towards the jet axis, where the velocity is highest. On the other hand, the large droplets travel rather near the shear layers.

6 Summary

The paper presents a numerical ILES study of a spark forced ignition in temporally evolving two-phase planar jet that is subjected to the strong shear forces acting at the shear layer, which along with growing turbulent fluctuations cause development of the large turbulent structures. The current parametric studies include examination of several different spark locations, two different initial droplets distributions and selected flow parameters, i.e. momentum thickness and jet Reynolds numbers. The obtained results allowed to formulate conclusions that are consistent with the findings from the previous studies on turbulent spray flames:

- marginal effect of streamwise spark locations is observed due to the low initial turbulence intensity and use of temporally developing jet configuration;
- the opposed is observed for the transversal spark locations; igniting very close to the droplets stream or within it can lead to the substantial heat absorption by the droplets, preventing formation of the high temperature kernel that would be sufficient to drive chemical reaction and heat release;
- igniting in regions of high strain rate can lead to the flame quenching even if fuel mass fraction does not exceed the flammability limits;
- hot kernel initiated in high Reynolds number flows is subjected to intense stretching, resulting in expansion of the heated region what causes heat diffusion into the greater volume thus decreasing the peak temperature;
- the flame firstly slides along the surface of the droplets stream until the spray is dispersed by the large flow structures and afterwards penetrates the spray;
- smaller droplets with lower Stokes numbers gather in the vicinity of the jet axis while larger droplets are shifted near the shear layers what augments the evaporation rates and fuel diffusion outside the spray stream.

Acknowledgements

This work was supported by grant 2015/17/B/ST8/03217 (National Science Centre, Poland) and statutory funds BS/PB-1-103-3010/11/P. PL-Grid infrastructure was used to carry out the computations.

References

Ahmed, S.; Mastorakos, E.: Spark ignition of lifted turbulent jet flames. *Combust. Flame*, 146, (2006), 215 – 231.

Chakraborty, N.; Mastorakos, E.: Direct numerical simulations of localised forced ignition in turbulent mixing layers: The effects of mixture fraction and its gradient. *Flow Turbul. Combust.*, 80, (2007), 155 – 186.

Duwig, C.; Nogenmyr, K.; Chan, C.; Dunn, M.: Large eddy simulations of a piloted lean premix jet flame using finite-rate chemistry. *Combust. Theor. Model.*, 15, (2011), 537 – 568.

Elghobashi, S.: On predicting particle-laden turbulent flows. *Appl. Sci. Res.*, 52, (1994), 309 – 329.

Fernandez-Tarrazo, E.; Sanchez, A.; Linan, A.; Williams, F.: A simple one-step chemistry model for partially premixed hydrocarbon combustion. *Combust. Flame*, 147, (2006), 32 – 37.

Hawkes, E.; Ramanan, S.; Sutherland, J.; Chen, J.: Scalar mixing in direct numerical simulations of temporally evolving plane jet flames with skeletal CO/H2 kinetics. *Proc. Combust. Inst.*, 31, (2007), 1633 – 1640.

Jones, W.; Prasad, V.: Large eddy simulation of the sandia flame series (d-f) using the eulerian stochastic field method. *Combust. Flame*, 157, (2010), 1621 – 1636.

Kuban, L.; Stempka, J.; Wawrzak, A.; Tyliszczak, A.: DNS and ILES study of ethanol spray forced-ignition in a time-evolving mixing layer. *MCS-10: Tenth Mediterranean Combustion Symposium*, Naples, 2017.

Lacaze, G.; Richardson, E.; Poinsot, T.: Large eddy simulation of spark ignition in a turbulent methane jet. *Combust. Flame*, 156, (2009), 1993 – 2009.

Mastorakos, E.: Forced ignition of turbulent spray flames. *Proc. Combust. Inst.*, 000, (2016), 1 – 17.

Miller, R.; Harstad, K.; Bellan, J.: Evaluation of equilibrium and non-equilibrium evaporation models for many-droplet gas-liquid flow simulations. *Int. J. Multiph. Flow*, 24, (1998), 1025 – 1055.

Neophytou, A.; Mastorakos, E.; Cant, R.: DNS of spark ignition and edge flame propagation in turbulent droplet-laden mixing layers. *Combust. Flame*, 157, (2010), 1071 – 1086.

O'Loughlin, W.; Masri, A.: A new burner for studying auto-ignition in turbulent dilute sprays. *Combust. Flame*, 158, (2011), 1577 – 1590.

Passot, T.; Pouquet, A.: Numerical simulation of compressible homogeneous flows in the turbulent regime. *J. Fluid Mech.*, 181, (1987), 441 – 466.

Schmidt, H.; Schumann, U.: Coherent structure of the convective boundary layer derived from large eddy simulation. *J. Fluid Mech.*, 200, (1989), 511 – 562.

Spalding, D.: The combustion of liquid fuels. *Proc. Combust. Inst.*, pages 847 – 864.

Stempka, J.: Impact of subgrid modelling and numerical method on autoignition simulation of two-phase flow. *Arch. Thermodyn.*, 39, (2018), 55 – 72.

Tyliszczak, A.: High-order compact difference algorithm on half-staggered meshes for low mach number flows. *Comput. Fluids*, 127, (2016), 131 – 145.

Vreman, W.: An eddy-viscosity subgrid-scale model for turbulent shear flow: Algebraic theory and applications. *Phys. Fluids*, 16, (2004), 3670 – 3681.

Wawrzak, A.; Tyliszczak, A.: LES-CMC simulations of a turbulent hydrogen jet in oxy-combustion regimes. *Int. J. Hydrogen Energ.*, 41, (2016), 9705 – 9717.

Address: Institute of Thermal Machinery, Czestochowa University of Technology, Faculty of Mechanical Engineering and Computer Science, Armii Krajowej 21, 42-201 Czestochowa, Poland
email: `stempka@imc.pcz.pl`